Applied Physics Express

The Japan Society of Applied Physics

LETTER

AlInN/GaN diodes for power electronic devices

Applied Physics Express 13, 091006 (2020)
https://doi.org/10.35848/1882-0786/abb180

LETTER

AlInN/GaN diodes for power electronic devices

Matthew R. Peart*, Damir Borovac, Wei Sun, Renbo Song, Nelson Tansu*, and Jonathan J. Wierer Jr.*

Center for Photonics and Nanoelectronics, Department of Electrical and Computer Engineering, Lehigh University, 7 Asa Dr., Bethlehem, PA 18015, United States of America

*E-mail: mrp211@lehigh.edu; tansu@lehigh.edu; jwierer@lehigh.edu

Received June 9, 2020; revised August 10, 2020; accepted August 21, 2020; published online September 4, 2020

AlInN/GaN power diodes consisting of a p-type GaN and a 300 nm thick n-type AlInN drift layer are demonstrated. The p–n junction is grown using metalorganic chemical vapor deposition, and the $Al_xIn_{1-x}N$ drift layer is lattice-matched to GaN ($x \sim 0.82$) with an electron concentration of $\sim 8 \times 10^{16}$ cm^{-3} after correcting for the 2-dimensional electron gas. The diodes exhibit ~ -60 V blocking capability. Under forward bias, the diode has a turn-on voltage of ~ 4 V. If experimental challenges are overcome, the ultrawide bandgap and high mobility of an AlInN drift layer could increase the performance of GaN-based power devices. © 2020 The Japan Society of Applied Physics

GaN-based vertical power devices are under development as higher-performance alternatives to conventional Si and SiC power devices. This research is driven by the availability of bulk GaN substrates and the advantages of GaN, which include higher power density, higher temperature of operation, faster-switching speed, and higher operating voltages that lead to enhanced efficiency in power circuits. The higher operating voltage of GaN is directly related to its wider bandgap and high critical electric fields. Now even wider bandgap semiconductors beyond GaN are beginning to be investigated. These so-called ultra-wide bandgap (UWBG) semiconductors include AlGaN,[1] Ga_2O_3,[2] diamond, cubic-BN,[3] and AlInN.[4]

For vertical power devices that operate at low switching frequencies, the semiconductors can be compared by the widely used Baliga's power figure of merit (FOM). It is defined as $V^2_{br}/R_{on\text{-}sp}$, where V_{br} is the maximum blocking voltage, and $R_{on\text{-}sp}$ is the specific on-resistance. The FOM can also be expressed alternatively as $¼\varepsilon\mu E_c^3$ where ε is the permittivity, μ is the mobility and E_c is the critical electric field which is the field intensity at which avalanche breakdown is initiated. Since the critical electric field increases as ~ 2.5 times the bandgap (E_g) the FOM $\sim (E_g)^6$, and these UWBG semiconductors have the potential for significantly higher performance in power devices.[3]

$Al_{0.82}In_{0.18}N$, which is lattice-matched to GaN, has been proposed as a further enhancement to GaN for vertical power devices[4] due to its wide bandgap (~ 4.4 eV) and high electron mobility (~ 450 cm^2 V^{-1} s^{-1}). These attributes lead to a potentially higher FOM at 33 GW cm^{-2} than GaN (14 GW cm^{-2}) and similar to those of Ga_2O_3 (37 GW cm^{-2}) and AlGaN (41 GW cm^{-2}).[4] The availability of GaN substrates provides AlInN with a low defect density substrate, and its proven ability for n- and p-type doping shows it has capabilities beyond other UWBG in the same class, such as Ga_2O_3 and AlGaN.[2,3,5]

The potential increase in performance by adding AlInN to GaN-based devices motivates experimental investigations. AlInN is still a relatively immature semiconductor with far fewer growth studies and device results compared to GaN, InGaN, and AlGaN. Growth studies have concentrated on morphology, microstructure, and impurities,[6–11] and n- and p-type doping.[5,12] In devices, AlInN has been primarily used in high-electron-mobility transistors,[7,8] for high index contrast layer in distributed Bragg reflectors,[9,10,12] as functional layers in LEDs or LDs,[13–16] thermoelectricity,[17] and solar-blind photodetectors.[5,13,18] There have been no reports of using AlInN in a power diode. Here, we demonstrate a quasi-vertical diode (a bipolar device) consisting of a highly doped p-type GaN and a low-doped n-type $Al_{0.82}In_{0.18}N$ drift layer formed on GaN templates as a prototype power diode.

The AlInN/GaN power diode is grown by metalorganic chemical vapor deposition on n-type GaN templates (formed on sapphire substrates) with an electron concentration of 5×10^{18} cm^{-3}. The growth of thick lattice-matched layers of AlInN on GaN is investigated first. A 300 nm thick and unintentionally doped AlInN layers are grown at 790 °C and 75 Torr. The group-III precursors are trimethylindium (TMIn) and trimethylaluminum (TMAl), and the growth uses a TMIn/TMAl molar flow ratio of ~ 1.65. The growth conditions produce relatively smooth AlInN surface morphology, with a root-mean-square roughness of ~ 3.5 nm, as is typical for the growth of AlInN on GaN/sapphire templates due to the formation of V-defects and threading dislocations.[10] X-ray reciprocal space mapping at the (20–25) reflection of the AlInN on GaN is shown in Fig. 1. The vertical alignment of the AlInN and GaN peaks indicate the AlInN drift layers are lattice-matched to the underlying GaN with an Al content of ~ 0.82. The carrier density and mobility of the AlInN layer measured by Hall measurement in the Van der Pauw configuration show n-type carrier concentrations of $n \sim 2 \times 10^{17}$ cm^{-3} and electron mobilities of $\mu_e \sim 370$ cm^2 V^{-1} s^{-1}. However, there is additional carriers included in the Hall measurement due to the 2-dimensional electron gas (2DEG) at the AlInN/GaN interface.[19] If the additional electrons within the 2DEG are removed using the calculations from Ref. 19 the electron concentration is corrected to $\sim 8 \times 10^{16}$ cm^{-3}. This carrier concentration is one of the lowest reported,[5,20] and secondary ion mass spectroscopy of the AlInN show the unintentional doping is caused by the incorporation of residual silicon in the growth chamber. Further details of the growth can be found in Ref. 19.

These low-doped and lattice-matched AlInN layers are then incorporated into the growth of the p–n junction structure shown in Fig. 2 to enable an AlInN power device and experimentally evaluate its voltage blocking capability. First, a 500 nm thick Si-doped n^+-GaN layer is grown on n-type GaN templates with an electron concentration of 5×10^{18} cm^{-3}. This layer is used for Ohmic contacting and current spreading because of the insulating substrate and top side contacting scheme. This layer was followed by the growth of a 300 nm thick unintentionally doped (n^-) AlInN

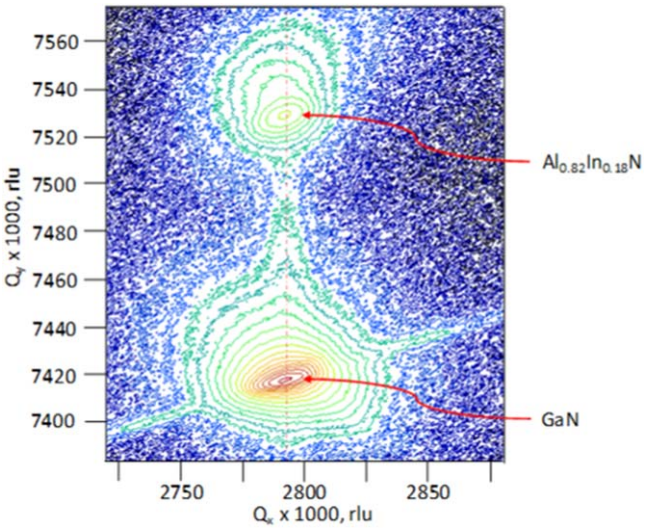

Fig. 1. (Color online) X-ray reciprocal space map at the (20–25) reflection. The peak of the GaN and AlInN are vertically aligned, demonstrating the AlInN is latticed matched to GaN.

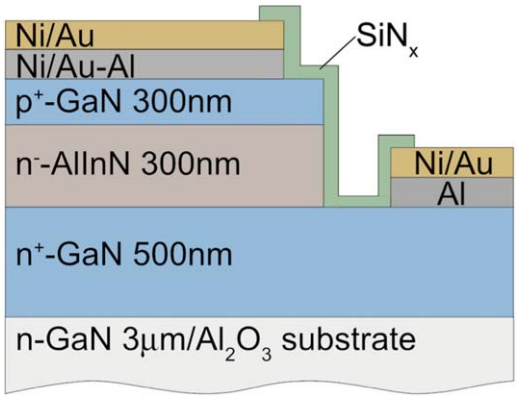

Fig. 2. (Color online) Schematic cross-section of the fabricated AlInN/GaN quasi-vertical power diode. A highly doped p^+-GaN layer and lightly doped n^--AlInN drift form the main junction. A highly doped n^+-GaN layer is for current spreading and cathode contacting.

drift layer. The AlInN layer was followed by a 300 nm thick, Mg-doped ($\sim 10^{19}$ cm^{-3}), p-type GaN layer grown at 950 °C and 200 T resulting in a hole concentration of 2×10^{17} cm^{-3}. Finally, growth is concluded by a thin (~20 nm) highly doped p-type GaN layer.

Following the growth, a simple fabrication process is performed to facilitate the electrical characterization of the diodes. First, 60 μm diameter circular p-contacts consisting of Ni/Au (15 nm/15 nm) are formed on the p-GaN by electron-beam evaporation and lithography liftoff. Then rapid thermal annealing is performed in N_2 at 600 °C for 1 min to ensure Ohmic contacts to the p-GaN. Then an inductively coupled plasma etch with Cl_2/BCl_3 to form 60 μm diameter circular mesas is performed to expose the underlying n^+-GaN contact layer. Next, 2000 nm of Al is deposited to form the cathode contact to the n^+-GaN that surrounds the circular mesa, and on top of the Ni/Au p-contact. This step is followed by depositing and patterning a Ni/Au (15 nm/100 nm) on both metal contacts for probing. Finally, a Si_3N_4 passivation layer is deposited by plasma-enhanced chemical vapor deposition and removed from the metal contact areas by reactive ion etching. A top-view image of the fabricated device after the formation of the Al contacts is shown in the inset of Fig. 3.

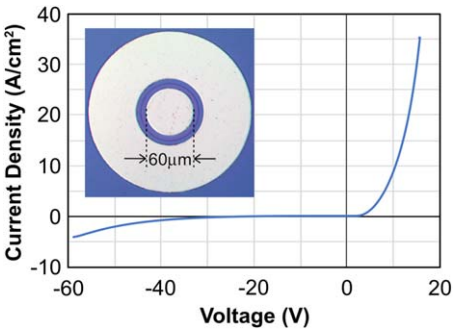

Fig. 3. (Color online) The forward and reverse current versus voltage characteristic. The inset shows a top-view microscope image of the device after the Al is deposited.

The fabricated devices are tested by wafer probing, and the current versus voltage (IV) characteristic is shown in Fig. 3. The AlInN/GaN p–n diodes are rectifying with an expected turn-on voltage ~4 V. Under reverse bias, the leakage current at −5 V is ~9 mA cm^{-2}. The reverse breakdown is limited by current leakage at ~−60 V. It is expected the leakage currents would improve with the use of low defect density GaN substrates. The maximum breakdown voltage is limited by the thickness of the AlInN drift region and is estimated by Eq. (1), where W_d is the width of the depletion region and the other variables are defined previously[21)]

$$V_{br} = \frac{1}{2} W_d E_c. \quad (1)$$

Assuming a critical electric field of 7.6 MV cm^{-1}[4)] and a drift layer thickness of 300 nm, the maximum predicted breakdown is 114 V. The $R_{on\text{-}sp}$ is 0.53 mohm cm^2 and is limited by the spreading resistance within the n^+-GaN contact layer and at the n-AlInN/n^+-GaN heterointerface.[4)]

The doping in the AlInN drift layer is verified using capacitance versus voltage measurements, as shown in Fig. 4. The analysis is made by fitting a line to the inverse of the capacitance squared ($1/C^2$), which results in two linear regions, the slopes of which provide measures of the carrier concentrations. The ~300 nm AlInN drift layer is depleted first, and a linear fit to the data gives a donor concentration

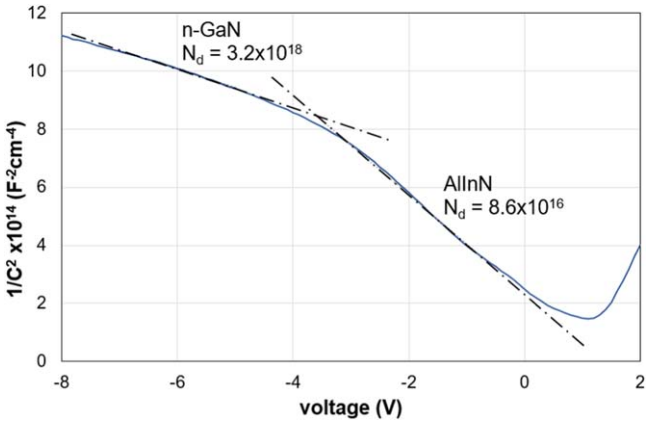

Fig. 4. (Color online) Inverse capacitance squared versus voltage characteristic for the AlInN/GaN power diode. The first linear region corresponds to a donor concentration (N_d) of 8.6×10^{16} cm^{-3} for the AlInN layer and $N_d = 3.2 \times 10^{18}$ cm^{-3} for the underlying n^+-GaN layer.

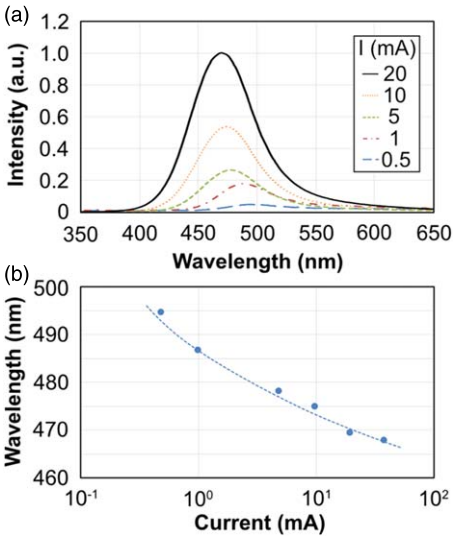

Fig. 5. (Color online) Electroluminescence of the AlInN/GaN diodes under forward bias. (a) Plot of intensity versus wavelength at different currents (I). (b) Plot of peak wavelength versus current. The data is the circles, and the dotted line is a guide for the eye.

(N_d) of $8.6 \times 10^{16}\,cm^{-3}$. This is among the lowest values reported and is within the measurement error compared to the electron concentration found in the Hall measurement when correcting for the 2DEG.[19] Under more substantial reverse bias, the n^+-GaN layer becomes depleted, and the measured donor concentration found in the second linear region is $3.2 \times 10^{18}\,cm^{-3}$. This is close to the targeted electron concentration of $5 \times 10^{18}\,cm^{-3}$. The additional electron concentration over donor concentration found by the Hall measurement for AlInN is possibly overestimated due to substrate conduction and the polarization induced 2DEG formed between the AlInN GaN interface.[19]

Under forward bias, strong visible electroluminescence is observed in all measured devices despite the lack of a layer with the appropriate bandgap in the structure. Plots of the spectra versus increasing current and peak wavelength versus current are shown in Figs. 5(a) and 5(b), respectively. While some electroluminescence is expected during forward bias due to band-to-band recombination, the measured wavelength range of 465–495 nm corresponds to bandgap energies of 2.51–2.67 eV, which is well below the bandgaps of GaN or AlInN at 3.4 and 4.4 eV, respectively.[22] The blue-shift with the increased current is similar to InGaN quantum well (QW) behavior in LEDs where injected free carriers screen the polarization fields between layers and reduce the quantum-confined Stark effect.

One possible explanation for this emission is the formation of an unintentional QW between the p^+-GaN and n-AlInN due to indium diffusion from the AlInN during the growth of the higher temperature p^+-GaN. Annealing AlInN layers at higher temperatures (>880 °C) under conditions similar to growth temperatures results in surface morphology changes that can be attributed to In loss.[15,23] During the growth of the p-GaN at 950 °C, some of the In is incorporated into this layer, forming the unintentional InGaN QW at the p-GaN/n-AlInN heterointerface. Even though this QW is unwanted, the band-to-band recombination in this layer does verify bipolar p–n junction operation.

There are other, but less likely, causes of this emission that could be considered. One possibility is due to recombination from states at the AlInN/GaN heterointerface where the severe band bending results in a lower bandgap.[24,25] However, emission from AlInN/GaN interfaces in Ref. 25 are at higher energies observed in this work. Another possibility is emission via defects that would also occur at lower energies, but this too would be highly unlikely because carriers should be lost via faster band-to band recombination rates.

In summary, a quasi-vertical p^+-GaN/n^--AlInN diode was fabricated, demonstrating for the first time the feasibility of AlInN for a bipolar power device. These initial results show rectification and good breakdown voltages despite the thin layers, but further experimental work will be required to optimize reverse leakage currents and lower $R_{on\text{-}sp}$. Improvements in reverse leakage and breakdown voltage will occur with growth on GaN substrates and the removal of the unintentional InGaN QW by controlling the p-type layer growth on the AlInN. Likewise, $R_{on\text{-}sp}$ will be significantly reduced once the lateral current spreading is removed by transitioning to bulk GaN substrates, and also by using interlayer and doping grading designs are incorporated to reduce the resistances from the AlInN/GaN heterojunction.

Acknowledgments The authors would like to acknowledge funding from US National Science Foundation (Awards # 1408051, 1505122, 1708227, and 1935295) and the Daniel E. ′39 and Patricia M. Smith Endowed Chair Professorship Fund (NT). The epitaxial growth and fabrication of the devices were performed at the Integrated Nanofabrication and Cleanroom Laboratory (INCL) at the Center for Photonics and Nanoelectronics (CPN).

ORCID iDs Matthew R. Peart https://orcid.org/0000-0001-9496-393X Jonathan J. Wierer Jr. https://orcid.org/0000-0001-6971-4835

1) A. M. Armstrong, M. P. King, R. J. Kaplar, A. J. Fischer, M. W. Moseley, J. J. Wierer, A. A. Allerman, M. H. Crawford, and J. R. Dickerson, Electron. Lett. **52**, 1319 (2016).
2) S. J. Pearton, J. Yang, P. H. Cary, F. Ren, J. Kim, M. J. Tadjer, and M. A. Mastro, Appl. Phys. Rev. **5**, 011301 (2018).
3) J. Y. Tsao et al., Adv. Electron. Mater. **4**, 1600501 (2018).
4) M. R. Peart, N. Tansu, and J. J. Wierer, IEEE Trans. Electron Devices **65**, 4276 (2018).
5) Y. Taniyasu, J. F. Carlin, A. Castiglia, R. Butté, and N. Grandjean, Appl. Phys. Lett. **101**, 2113 (2012).
6) M. Miyoshi, M. Yamanaka, T. Egawa, and T. Takeuchi, Appl. Phys. Express **11**, 051001 (2018).
7) M. Miyoshi, M. Yamanaka, T. Egawa, and T. Takeuchi, Jpn. J. Appl. Phys. **58**, SC1006 (2019).
8) M. Miyoshi, M. Yamanaka, T. Egawa, and T. Takeuchi, J. Cryst. Growth **506**, 40 (2019).
9) V. Portz, M. Schnedler, M. Duchamp, F. M. Hsiao, H. Eisele, J. F. Carlin, R. Butté, N. Grandjean, R. E. Dunin-Borkowski, and P. Ebert, Appl. Phys. Lett. **109**, 132102 (2016).
10) R. B. Chung, F. Wu, R. Shivaraman, S. Keller, S. P. Denbaars, J. S. Speck, and S. Nakamura, J. Cryst. Growth **324**, 163 (2011).
11) S. Yamaguchi, M. Kariya, S. Nitta, H. Kato, T. Takeuchi, C. Wetzel, H. Amano, and I. Akasaki, J. Cryst. Growth **195**, 309 (1998).
12) M. A. Py, L. Lugani, Y. Taniyasu, J. F. Carlin, and N. Grandjean, J. Appl. Phys. **117**, 7501 (2015).
13) A. T. Cheng, Y. K. Su, W. C. Lai, Y. Z. Chen, and S. Y. Kuo, J. Electron. Mater. **37**, 1070 (2008).
14) A. Castiglia, E. Feltin, J. Dorsaz, G. Cosendey, J. F. Carlin, R. Butté, and N. Grandjean, Electron. Lett. **44**, 521 (2008).
15) W. Sun, S. A. Al Muyeed, R. Song, J. J. Wierer, and N. Tansu, Appl. Phys. Lett. **112**, 201106 (2018).
16) K. Arakawa, K. Miyoshi, R. Iida, Y. Kato, T. Takeuchi, M. Miyoshi, S. Kamiyama, M. Iwaya, and I. Akasaki, Jpn. J. Appl. Phys. **58**, SCCC28 (2019).
17) J. Zhang, H. Tong, G. Liu, J. A. Herbsommer, G. S. Huang, and N. Tansu, J. Appl. Phys. **109**, 053706 (2011).
18) W. Y. Weng, S. J. Chang, W. C. Lai, T. J. Hsueh, S. C. Shei, X. F. Zeng, S. L. Wu, and S. C. Hung, IEEE Photonics Technol. Lett. **21**, 504 (2009).

19) D. Borovac, W. Sun, M. R. Peart, R. Song, N. Tansu, and J. J. Wierer, to be published in J. Cryst. Growth (2020).
20) G. Liu, J. Zhang, X. H. Li, G. S. Huang, T. Paskova, K. R. Evans, H. Zhao, and N. Tansu, J. Cryst. Growth **340**, 66 (2012).
21) B. J. Baliga, *Fundamentals of Power Semiconductor Devices* (Springer, New York, 2008), p. 15.
22) R. Butté et al., J. Phys. D **40**, 6328 (2007).
23) D. Borovac, W. Sun, R. Song, J. J. Wierer, and N. Tansu, J. Cryst. Growth **533**, 125469 (2020).
24) L. Li, D. Hosomi, Y. Miyachi, M. Miyoshi, and T. Egawa, Appl. Phys. Lett. **112**, 102102 (2018).
25) M. F. Romero, M. Feneberg, P. Moser, C. Berger, J. Bläsing, A. Dadgar, A. Krost, E. Sakalauskas, and R. Goldhahn, Appl. Phys. Lett. **100**, 212101 (2012).